

Adiabatic Continuity Between Hofstadter and Chern Insulators

Ying-Hai Wu,¹ J. K. Jain,¹ and Kai Sun²

¹ *Department of Physics, 104 Davey Lab, The Pennsylvania State University, University Park, PA 16802 and*

² *Condensed Matter Theory Center and Joint Quantum Institute,*

Department of Physics, University of Maryland, College Park, MD 20742

(Dated: March 21, 2019)

We show that the topologically nontrivial bands of Chern insulators are adiabatic cousins of the Landau bands of Hofstadter lattices. We demonstrate adiabatic connection also between the familiar fractional quantum Hall states on Hofstadter lattices and the fractional Chern insulator states in partially filled Chern bands, which implies that they are in fact different manifestations of the same phase. This adiabatic path provides a way of generating many more fractional Chern insulator states, and helps clarify that non-uniformity in the distribution of the Berry curvature is responsible for weakening or altogether destroying fractional topological states.

Introduction – While Landau levels have been known since 1930, it was only in 1976 that Hofstadter [1] studied a periodic lattice with a rational number of flux quanta passing through each plaquette, where the Landau levels are recovered in the small flux quanta limit. In 1982, it was shown by Thouless, Kohmoto, Nightingale and den Nijs [2] that the Hall conductance of a filled Hofstadter band is a topological index: the first Chern number C . Subsequently, a model on the honeycomb lattice with $C = 1$ was proposed by Haldane [3] which has a nonzero Chern number in zero *net* magnetic field. Such a zero net field lattice system is now referred to as a Chern insulator, to distinguish it from the quantum Hall insulators obtained in a uniform magnetic field. It is a natural question whether Chern insulators can also host strongly correlated fractional quantum Hall (FQH) like states, referred to as fractional Chern insulator (FCI) states. Recently, Chern insulators with nearly-flat bands have been proposed [4–6], in which FCIs have been reported at filling factors $\nu = 1/3$ [7–9], $1/2$ [10], $2/5$ and $3/7$ [11] for fermions, and $1/2$ [12], 1 [13] and $2/3$ [11] for bosons. Trial wavefunctions for FCIs have been proposed [14–16]. Flatband models with $C > 1$ have also been constructed and produce strongly-interacting topological states [17–21]. While the FCI states appear similar to the FQH states found in the lowest Landau level, no direct connection between them has yet been established, and it remains unclear to what extent the extensive physics of the FQH effect and composite fermions [22, 23] is possible in Chern insulators. Progress in this direction has been made by Murthy and Shankar [24], who exploit the modified algebra of the density operator projected into the lowest Chern band to motivate composite fermion (CF) physics [25].

We address below this issue by demonstrating an adiabatic continuity between the bands of a Hofstadter lattice and a Chern insulator. We observe that, in fact, there is no fundamental distinction between Hofstadter and Chern insulators, because the former can be turned into the latter by a gauge transformation. This implies that all of the physics of FQH effect and composite fermions

is, in principle, possible for Chern insulators, provided that we allow Chern insulators with sufficiently complex unit cells. For simpler Chern lattices, however, not all FQH states survive. We consider certain previously introduced Chern insulators and show, using exact numerical methods, that the familiar FQH states at filling factors $1/3$ and $1/2$ of the Hofstadter model adiabatically evolve into the corresponding FCI states in the presence of appropriate repulsive interactions. This also makes it apparent that the filling fraction of the lowest band of the FCIs corresponds to the filling factor of the lowest Landau level. In addition to establishing that the origin of these states is governed by the same underlying physics, this adiabatic connection also enables us to investigate the role of the Berry curvature distribution (in the momentum space). We find that non-uniformity in the distribution of the Berry curvature weakens and can even destroy FQH states. Our results show that such non-uniformities effectively translate into an enhancement of the residual interaction between composite fermions, and as a result can eliminate states of the sequence $p/(2p \pm 1)$ with relatively small gaps (all these fractions occur for noninteracting composite fermions). As a byproduct, our work provides a natural way to generate Chern insulators with an arbitrarily flat Berry curvature.

Hofstadter and Checkerboard Lattice Models – We first study the single-particle band structures to demonstrate the adiabatic connection between a Landau level and a topological flatband using a specific model as an example. The construction is generic and straightforwardly generalizable to other models; another model is presented in the Supplementary Material (SM).

We consider the Hofstadter Hamiltonian H_{sq} on a square lattice with nearest neighbor hopping and a magnetic flux $2\pi/n$ through each square. In the weak lattice limit ($n \gg 1$), Landau levels are recovered. An example with $n = 16$ is shown (dots) in Fig. 1a, which also depicts the “checkerboard” lattice with its two sublattices marked by blue and red rectangles. As shown in Refs. [5, 7], the checkerboard lattice supports a topological flatband in the presence of nearest-neighbor, next-nearest-

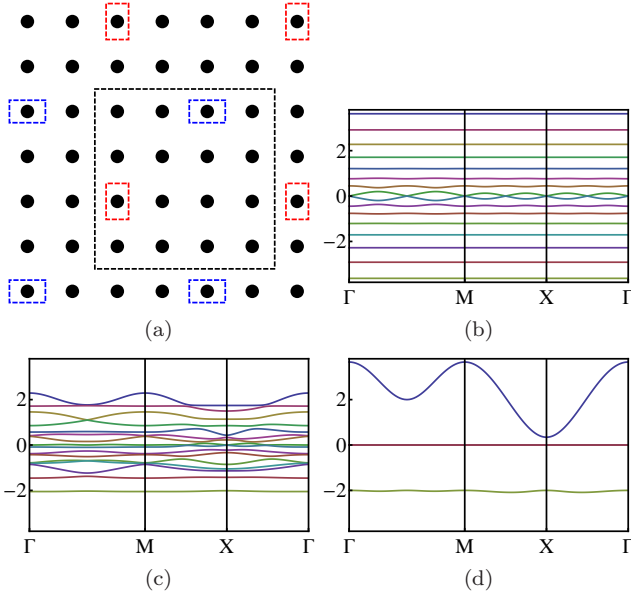


FIG. 1. Lattice model and band structure. Fig. (a) shows the lattice we studied. The black dots show the lattice sites in a Hofstadter lattice with flux $2\pi/16$ through each plaquette. The dashed black square marks a magnetic unit cell containing 16 sites. The sites marked by the dashed rectangles form a checkerboard lattice where the two different orientations of the rectangles represent two sublattices. The Hamiltonian $H_{cs}(R)$ in Eq. (1) interpolates between the Hofstadter and Chern insulator limits as R is varied from 0 to 1. Panels (b-d) show the band structures at three values of R (0, 0.5 and 1, respectively) along the contour $\Gamma \rightarrow M \rightarrow X \rightarrow \Gamma$ in the momentum space. In (b), flat Landau levels carry Chern number $C = 1$ while the two non-flat bands at the middle have $C = -14$. In (d), the top and bottom bands of the checkerboard model have nontrivial Chern numbers $C = \mp 1$.

neighbor and next-next-nearest-neighbor hoppings, with the nearest neighbor hopping carrying nonzero complex phase. We refer to this checkerboard Hamiltonian as H_{cb} , and define an interpolating Hamiltonian (with parameters and gauge choice given in SM)

$$H_{cs}(R) = RH_{cb} + (1 - R)H_{sq}, \quad (1)$$

which evolves continuously from Hofstadter to checkerboard as R increases from 0 to 1. Along this path, explicit calculation shows that the lowest band always remains gapped, which implies that the lowest Landau level of the Hofstadter model adiabatically evolves into the lowest band of the Chern insulator, carrying along its Chern number. In addition, the bandwidth of the lowest band is small for any R , indicating that it remains flat throughout its evolution. In SM, we show that similar connection can be found between a Hofstadter triangular lattice and the kagome lattice flatband model presented in Ref. [4].

An intuitive understanding can be gained by noting that a Hofstadter insulator in a *uniform* magnetic field can be turned into a Chern insulator in zero *net* mag-

netic field by a simple gauge transformation. For a Hofstadter lattice, the total magnetic field passing through each magnetic unit cell is $2q\pi$ (q integer). If we insert a $-2q\pi$ flux at an arbitrary point in each magnetic unit cell, and treat the magnetic unit cell as our (enlarged) unit cell, the total magnetic field through this enlarged unit cell vanishes. The insertion of the $\pm 2q\pi$ flux in a tight-binding model, however, is simply a gauge choice that has no physical consequence, and hence leaves all properties of the system unchanged, including all bands and their Chern numbers, thus producing a Chern insulator with flat bands and uniform Berry curvature. This shows that no fundamental distinction exists between a QH insulator and a Chern insulator, thus bringing out the fundamental reason why an adiabatic connection between these two types of states is possible.

Fractional Quantum Hall Effect – A Hofstadter lattice with sufficiently small flux per plaquette simulates the continuum, and thus displays all of the standard FQH states. Given that a Hofstadter insulator can trivially be converted into a Chern insulator, it follows, in principle, that all of this physics is possible also for Chern insulators, provided one chooses a sufficiently detailed unit cell. For a given Chern insulator, however, not all FQH states may occur. In other words, as we go from the Hofstadter insulator to a given Chern insulator by adiabatically switching off certain sites, not all FQH states will survive. Our exact diagonalization results below show, within the context of the checkerboard lattice, that the $1/3$ Laughlin state [26] and the $1/2$ Moore-Read state [27] survive. We show in the SM results about the $2/5$ Jain state on the checkerboard lattice and the $1/3$ and $1/2$ states on the kagome lattice.

Following standard practice [8], we project out all high energy bands to reduce the size of the Hilbert space, and set the width of the lowest band to zero to eliminate the effect of the band curvature. As for the interaction, at $1/3$ filling, we use an interaction that decays as $1/r^2$ for $r \leq r_c$ and vanishes for $r > r_c$, with r_c chosen to produce a nearest neighbor interaction in the Chern insulator limit. At $\nu = 1/2$, we consider an interaction (see SM for details) that reduces to a nearest neighbor three-body interaction in the Chern insulator limit. The number of particles is N , and the lattice sites in the x - and y -directions are labeled N_x and N_y . The many body eigenstates are indexed by the momentum (K_x, K_y) (integers in units of $2\pi/L$), defined modulo (N_x, N_y) . In the valence band, the many body Slater basis states are given by $\prod_{i=1}^N \gamma_{V, \vec{k}_i}^\dagger \cdots \gamma_{V, \vec{k}_N}^\dagger |0\rangle$ where $\gamma_{V, \vec{k}}^\dagger$'s are the creation operators for a particle of momentum \vec{k} in the valence band.

We demonstrate adiabatic connectivity by considering the ground state, quasi-hole and the quasiparticle spectra, and also their particle entanglement spectra [28] as a function of R . Our calculations below show that they

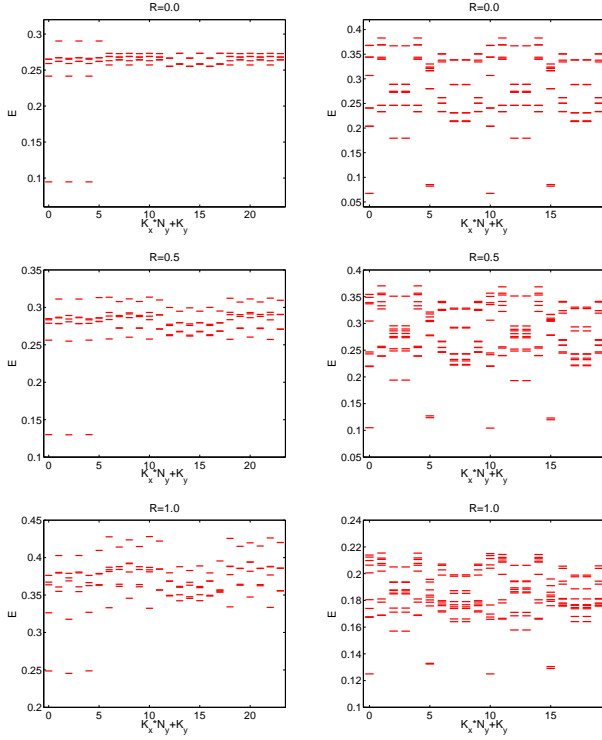


FIG. 2. Energy spectra at filling $1/3$ (left) and $1/2$ (right) for $R = 0.0, 0.5$ and 1.0 (top to bottom). In the left panels, there are 3 quasi-degenerate states at $(K_x, K_y) = (0, 0), (0, 2)$ and $(0, 4)$. In the right panels, there are 6 quasi-degenerate states: one each at $(K_x, K_y) = (0, 0)$ or $(2, 0)$, and two for $(1, 0)$ or $(3, 0)$. The system size is 4×6 (4×5) for $1/3$ ($1/2$) filling.

all evolve adiabatically from the Hofstadter model to the Chern flatband model with the counting of states in agreement with the folding rule given by Bernevig and Regnault [10].

Fig. 2 shows the energy spectra at $1/3$ ($N = 8$, $N_x = 4$ and $N_y = 6$) and $1/2$ ($N = 10$, $N_x = 4$ and $N_y = 5$) fillings with $R = 0.0, 0.5$ and 1.0 . For $1/3$ filling, we observe 3 quasi-degenerate states at $(K_x, K_y) = (0, 0), (0, 2)$ and $(0, 4)$, while 6 quasi-degenerate states are found at $1/2$ filling: one for $(K_x, K_y) = (0, 0)$ or $(2, 0)$ and two for $(1, 0)$ or $(3, 0)$. These results are consistent with the prediction of the root partition and folding rule [10]. Importantly, the gap does not close as R is increased from 0 to 1, as shown in Fig. 3. It is shown in the SM that the quasi-degenerate ground states evolve into one another upon flux insertion along the y - or x -direction but they do not cross levels with higher energy states.

In Fig. 4, the quasihole spectra with $N = 7$, $N_x = 4$ and $N_y = 6$ ($N = 10$, $N_x = 3$ and $N_y = 7$) are presented, which corresponds to a $\nu = 1/3$ ($\nu = 1/2$) state with three (two) quasiholes. There are 12 (6) low energy states in each momentum sector for $1/3$ ($1/2$) filling, again in agreement with theoretical predictions [10]. The gap between the low energy quasihole manifold and the

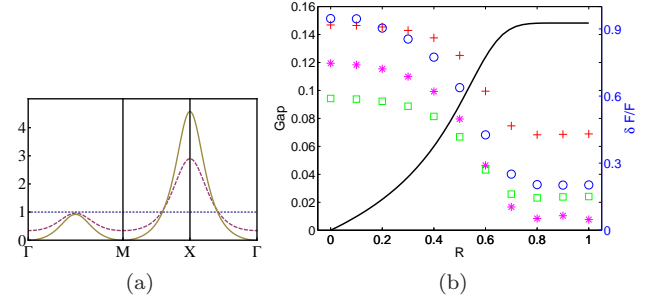


FIG. 3. Berry curvature distribution for the lowest band and various gaps. (a) The Berry curvature at different \mathbf{k} -points with $R = 0.0, 0.5$ and 1.0 (dotted, dashed and solid lines respectively). (b) The plus signs, circles, squares and asterisks show the gaps in the spectra of the $1/3$ ground states, $1/3$ quasihole states, $1/2$ ground states, and $1/2$ quasihole states at several R . The continuous line shows the deviation of the Berry curvature $\delta\mathcal{F}$ (normalized by the average value $\bar{\mathcal{F}}$) as a function of R .

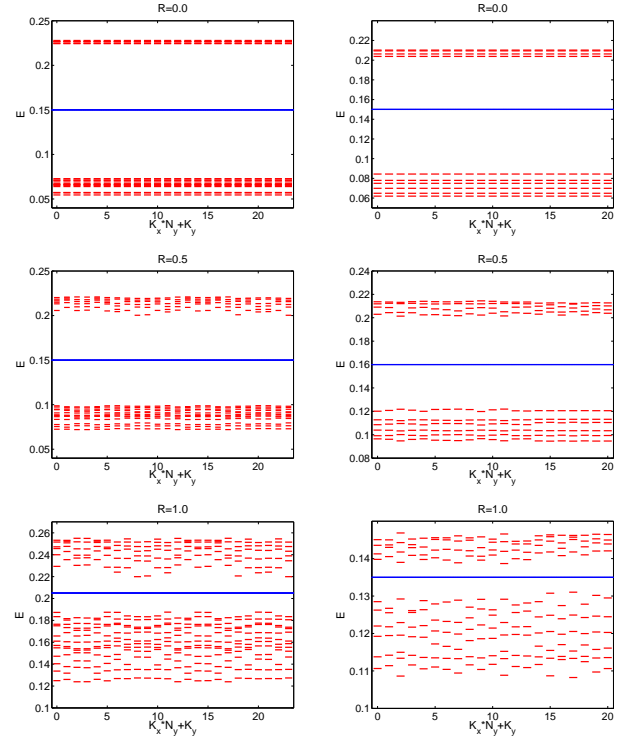


FIG. 4. Quasihole spectra at $1/3$ (left) and $1/2$ (right) fillings at $R = 0.0, 0.5$ and 1.0 (top to bottom). There are 12 (6) states in the low energy manifold (below the blue lines) in each momentum sector for the left (right) column.

higher energy states also does not close, as shown by the circles and asterisks in Fig. 3. The quasiparticle spectra show similar behavior (see SM).

Finally, the particle entanglement spectra are presented in Fig. 5 for $1/3$ and $1/2$ fillings. We trace out 5 and 6 particles in these two cases, respectively (see SM

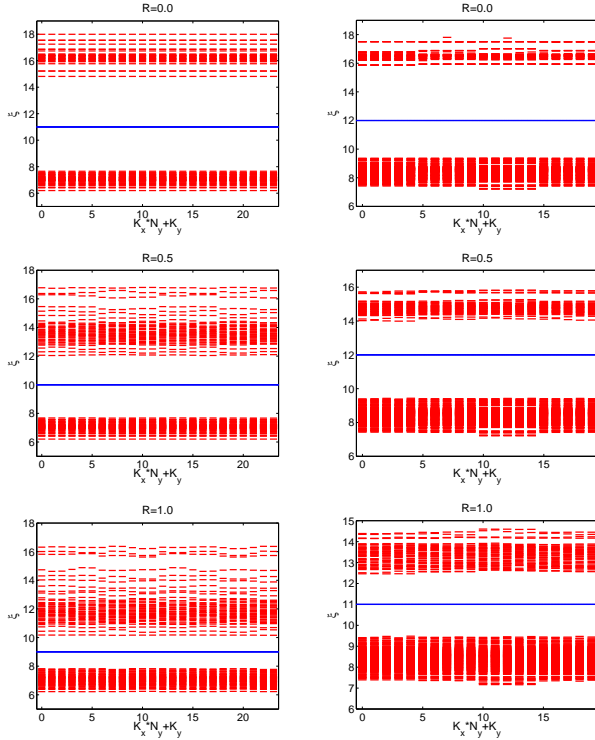


FIG. 5. Particle entanglement spectra at 1/3 (left) and 1/2 (right) with $R = 0, 0.5$ and 1 (top to bottom). In the left column, the number of states in the low entanglement energy manifold indicated by the blue lines are 46 states in the $K_y = 0, 3$ momentum sectors and 45 states in other sectors. In the right column, the number of states in the low entanglement energy manifold indicated by the blue lines are 200, 196, 201 and 196 states in the $K_x = 0, 1, 2$ and 3 momentum sectors, respectively.

for more details). In the left column (1/3 filling), the low energy band (below the blue lines) consists of 46 states at each momentum in the $K_y = 0, 3$ momentum sectors and 45 states in other sectors. In the right column (1/2 filling), the low energy band has 200, 196, 201 and 196 states in the $K_x = 0, 1, 2$ and 3 momentum sectors, respectively. The counting also agrees with the predictions given by root partition and folding rule [10] and the entanglement gap does not close for any value of R .

The Distribution of Berry Curvature – The adiabatic path between a FQHI and a FCI offers a natural way to explore the role of the distribution of the Berry curvature in the momentum space. As R is increased from 0 to 1, the lowest band shows little change in terms of the band structure, but its Berry curvature (\mathcal{F}) changes dramatically. As shown in Fig. 3a, for our model, the Berry curvature of the lowest band is flat at $R = 0$, as expected for a Landau level. However, as R increases, the value of \mathcal{F} reduces near the Γ and M points, and has a peak at X . Although the integrated Berry curvature in the whole Brillouin zone remains constant (2π times the Chern number), its deviation $\delta\mathcal{F}$ (see SM for defini-

tion) becomes nearly as large as its mean value ($\bar{\mathcal{F}}$) as R approaches unity.

This change in the distribution of the Berry curvature has a direct correlation with the many body properties. We see from Fig. 3b that the spectral gaps for the ground and quasihole states at different fillings follow the same trend, changing rapidly for $R < 0.7$ and then saturating at $R \sim 0.7$. These many-body gaps show no obvious correlation with single-particle quantities, such as the bandwidth and the band gap of the lowest band (shown in SM), but have a strong (anti)correlation with $\delta\mathcal{F}$ (Fig. 3), indicating its important role in the FCI states. While the topological properties remain intact over a wide range of $\delta\mathcal{F}$, an increase in $\delta\mathcal{F}$ reduces the size of the gap and thus the robustness of the FCI states. As shown in the SM, we have found that the bandwidth of the quasihole states increases with $\delta\mathcal{F}$, indicating that larger $\delta\mathcal{F}$ implies stronger short range interaction between (CF) quasiholes.

Conclusion – We have shown, by studying the ground states, quasihole and quasiparticle states, and their particle entanglement spectra, that the integer and fractional states in the Hofstadter and Chern insulators are adiabatically connected. Our study reveals that the nonuniform distribution of the Berry curvature reduces the gap and increases the interaction strength between quasiparticles. In addition, our work shows how Chern insulators with arbitrarily uniform Berry curvature can be constructed by allowing more complex lattices, which should produce many other FCI states. Time reversal invariant fractional topological insulators can be constructed from the $p/(2p+1)$ states by introducing a spin, and are expected to be topologically stable for odd p [29].

Acknowledgements – We are indebted to the authors, especially N. Regnault, of the DiagHam package, and acknowledge financial support from the JQI-NSF-PFC (KS) and the DOE Grant no. de-sc0005042 (YHW and JKJ). YHW and JKJ thank the Joint Quantum Institute and the Condensed Matter Theory Center, University of Maryland, for their kind hospitality.

Note added – At the time of finalizing the manuscript, we became aware of a preprint [31] on a similar topic.

-
- [1] D. R. Hofstadter, Phys. Rev. B **14**, 2239 (1976).
 - [2] D. J. Thouless, M. Kohmoto, M. P. Nightingale, and M. den Nijs, Phys. Rev. Lett. **49**, 405 (1982).
 - [3] F. D. M. Haldane, Phys. Rev. Lett. **61**, 2015 (1988).
 - [4] E. Tang, J.-W. Mei, and X.-G. Wen, Phys. Rev. Lett. **106**, 236802 (2011).
 - [5] K. Sun, Z. Gu, H. Katsura, and S. Das Sarma, Phys. Rev. Lett. **106**, 236803 (2011).
 - [6] T. Neupert, L. Santos, C. Chamon, and C. Mudry, Phys. Rev. Lett. **106**, 236804 (2011).
 - [7] D. N. Sheng, Z.-C. Gu, K. Sun, and L. Sheng, Nat.

Comm. **2**, 389 (2011).

- [8] N. Regnault and B. A. Bernevig, Phys. Rev. X **1**, 021014 (2011).
- [9] Y.-L. Wu, B. A. Bernevig, and N. Regnault, Phys. Rev. B **85**, 075116 (2012).
- [10] B. A. Bernevig and N. Regnault, Phys. Rev. B **85**, 075128 (2012).
- [11] T. Liu, C. Repellin, B. A. Bernevig and N. Regnault, arXiv:1206.2626
- [12] Y.-F. Wang, H. Yao, Z.-C. Gu, C.-D. Gong, and D. N. Sheng, Phys. Rev. Lett. **108**, 126805 (2012).
- [13] Y.-F. Wang, Z.-C. Gu, C.-D. Gong, and D. N. Sheng, Phys. Rev. Lett. **107**, 146803 (2011).
- [14] X.-L. Qi, Phys. Rev. Lett. **107**, 126803 (2011).
- [15] Y.-M. Lu and Y. Ran, Phys. Rev. B. **85**, 165134 (2012)
- [16] Y.-L. Wu, B. A. Bernevig, and N. Regnault, arXiv: 1206.5773
- [17] F. Wang and Y. Ran, Phys. Rev. B **84**, 241103(R) (2011).
- [18] Y.-F. Wang, H. Yao, C.-D. Gong, and D. N. Sheng, arXiv:1204.1697.
- [19] M. Trescher and E. J. Bergholtz, arXiv:1205.2245.
- [20] Z. Liu, E. J. Bergholtz, H. Fan, and A. M. Läuchli, arXiv:1206.3759.
- [21] S. Yang, Z.-C. Gu, K. Sun and S. Das Sarma, arXiv:1205.5792.
- [22] *Perspectives in Quantum Hall Effects*, eds. S. Das Sarma and A. Pinzucuk (Wiley, New York, 1997).
- [23] *Composite Fermions*, J.K. Jain (Cambridge University Press, 2007).
- [24] G. Murthy and R. Shankar, arXiv:1108.5501 (2011); arXiv:1207.2133 (2012).
- [25] J. K. Jain, Phys. Rev. Lett. **63**, 199 (1989); Phys. Rev. B **41**, 7653 (1990).
- [26] R. B. Laughlin, Phys. Rev. Lett. **50**, 1395 (1983).
- [27] G. Moore and N. Read, Nucl. Phys. B **360**, 362 (1991).
- [28] A. Sterdyniak, N. Regnault and B. A. Bernevig, Phys. Rev. Lett. **106**, 100405 (2011).
- [29] D. Ferraro and G. Viola, arXiv:1112.5399 (2012).
- [30] B. A. Bernevig and F. D. M. Haldane, Phys. Rev. Lett. **100**, 246802 (2008).
- [31] T. Scaffidi and G. Moller, arXiv:1207.3539 (2012).

Supplementary Material

We supply here details of the checkerboard lattice model, and also the analysis on the kagome lattice model.

CHECKERBOARD LATTICE MODEL

For the square lattice model shown in Fig. 1(a), each unit cell contains sixteen lattice sites and are labeled by (μ, ν) where $\mu, \nu \in \{0, 1, 2, 3\}$. The index of a site is defined as $i = \mu + 4\nu$ which increases from left to right and then bottom to top. In the Hofstadter Hamiltonian $H_{\text{sq}} = -\sum_{\mu\nu, \sigma\rho} t_{\mu\nu, \sigma\rho} c_{\mu\nu}^\dagger c_{\sigma\rho}$, $c_{\mu\nu}^\dagger$ is the creation operator on the site (μ, ν) and only nearest-neighbor hopping is allowed, *i.e.*, $t_{\mu\nu, \sigma\rho}$ is non-zero only if $\mu = \sigma \pm 1, \nu = \rho$ or $\mu = \sigma, \nu = \rho \pm 1$. Note that μ is defined modulo 4. The hopping amplitudes $t_{\mu\nu, \mu+1\nu}$ and $t_{\mu\nu, \mu\nu+1}$ are given by $\exp(i\phi_{\mu\nu}^X)$ and $\exp(i\phi_{\mu\nu}^Y)$, respectively. The other components can be fixed by requiring the full Hamiltonian to be Hermitian. The gauge is fixed by requiring $\phi_{\mu, \nu}^X = \phi_{\mu, \nu}^Y = \phi_{3-\nu, 3-\mu}^X = \phi_{3-\nu, 3-\mu}^Y$, and we get

$$\begin{aligned} \phi_{0,0}^X &= \frac{3\pi}{80} & \phi_{0,1}^X &= \frac{3\pi}{40} & \phi_{0,2}^X &= \frac{\pi}{16} & \phi_{0,3}^X &= 0 \\ \phi_{1,0}^X &= \frac{\pi}{5} & \phi_{1,1}^X &= \frac{19\pi}{80} & \phi_{1,2}^X &= \frac{7\pi}{40} & \phi_{1,3}^X &= \frac{\pi}{16} \\ \phi_{2,0}^X &= \frac{37\pi}{80} & \phi_{2,1}^X &= \frac{2\pi}{5} & \phi_{2,2}^X &= \frac{19\pi}{80} & \phi_{2,3}^X &= \frac{3\pi}{40} \\ \phi_{3,0}^X &= \frac{39\pi}{40} & \phi_{3,1}^X &= \frac{37\pi}{80} & \phi_{3,2}^X &= \frac{\pi}{5} & \phi_{3,3}^X &= \frac{3\pi}{80} \end{aligned}$$

The checkerboard lattice Hamiltonian [5] is $H_{\text{cb}} = -\sum_{\mu\nu, \sigma\rho} \tilde{t}_{\mu\nu, \sigma\rho} c_{\mu\nu}^\dagger c_{\sigma\rho} = \sum_{\vec{k}, ij} \mathcal{H}_{ij}(\vec{k}) c_i^\dagger(\vec{k}) c_j(\vec{k})$, where $i = \mu + 4\nu$ and $j = \sigma + 4\rho$. The non-zero components of \mathcal{H}_{ij} are $\mathcal{H}_{44} = (-2t_2)(\cos(k_x + 7\pi/40) + \cos(k_y + 47\pi/40)) + 2t_3(\cos(k_x + k_y + 47\pi/20) + \cos(k_x - k_y))$, $\mathcal{H}_{14,14} = (-2t_2)(\cos(k_x + 7\pi/40) + \cos(k_y + 47\pi/40)) + 2t_3(\cos(k_x + k_y + 47\pi/20) + \cos(k_x - k_y))$, $\mathcal{H}_{4,14} = (-t_1)(\exp(k_x/2 + k_y/2 + 3\pi/8) + \exp(-k_x/2 + k_y/2 - 3\pi/10) + \exp(-k_x/2 - k_y/2 - 79\pi/40) + \exp(k_x/2 - k_y/2 - 3\pi/10))$ and $\mathcal{H}_{14,4} = (\mathcal{H}_{4,14})^*$, where $t_1 = 1$, $t_2 = 1 - \sqrt{2}/2$ and $t_3 = (\sqrt{2} - 1)/2$.

The deviation of Berry curvature is defined as

$$\delta\mathcal{F} = \sqrt{\int_{\text{BZ}} dk_x dk_y (\mathcal{F}(k_x, k_y) - \bar{\mathcal{F}})^2} \quad (\text{S1})$$

where $\bar{\mathcal{F}}$ is the average of the Berry curvature.

We use a two body interaction Hamiltonian $H_2 = \sum_{[i,j]} U_{ij} \hat{n}_i \hat{n}_j$ at $1/3$ and a three body interaction Hamiltonian $H_3 = \sum_{[i,j,k]} V_{ijk} \hat{n}_i \hat{n}_j \hat{n}_k$ at $1/2$, where $\hat{n}_i = c_i^\dagger c_i$ is the particle number operator on site i , $U_{ij} = 0.5/r_{ij}^2$ and $V_{ijk} = 0.5/(r_{ij} r_{jk} r_{ki})^2$, where r_{ij} is the distance between the sites i and j . The summation in H_2 is over all pairs i, j for which $r_{ij} \leq \sqrt{2}/2$ and that in H_3 is over all combinations of i, j, k for which $r_{ij, jk, ki} \leq 1$ and

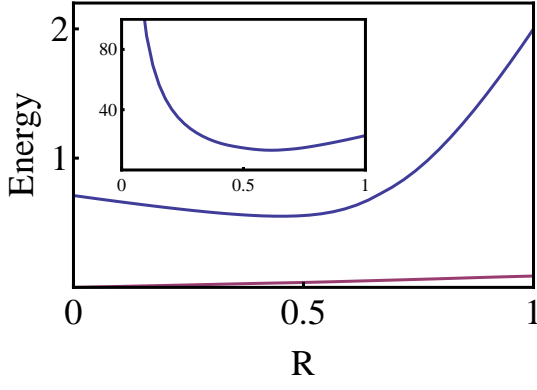


FIG. S1. The single-particle band gap (top curve) and band-width (lower curve) as a function of R . The flatness ratio (band gap over bandwidth) is shown in the inset.

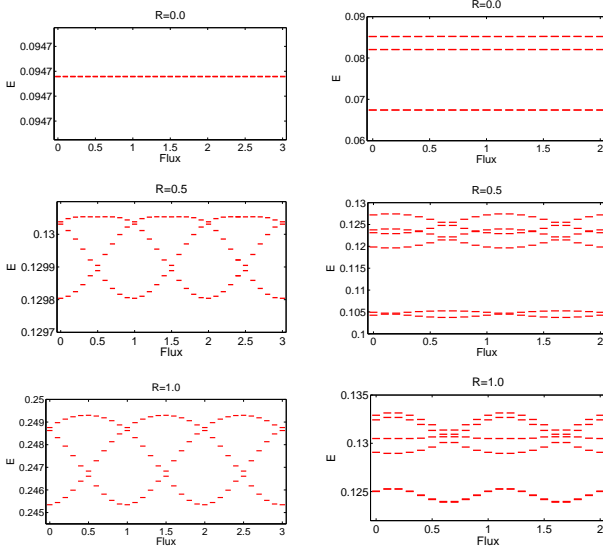


FIG. S2. Evolution of the 1/3 (left) and 1/2 (right) ground states shown in Fig. 2 in the main text upon flux insertion in the y -direction and x -direction, respectively. In both cases, the quasi-degenerate ground states are separated from the excited state at each point. Note that at $R = 0.0$, the states are perfectly degenerate at each flux value and there is no obvious spectral flow.

$r_{ij}r_{jk}r_{ki} \leq 1/2$. All distances here are quoted in units of the lattice constant of the magnetic unit cell.

Fig. S1 shows the single-particle band gap and band-width as a function of R . Fig. S2 shows that the quasi-degenerate ground states evolve into one another upon flux insertion along the y - or x -direction but there is no level crossing with higher energy states. Fig. S3 shows the energy splittings of the nearly degenerate ground states, as well as the quasihole states for 1/3 and 1/2 fillings.

To calculate the particle entanglement spectrum (PES) [28], we define the density matrix as $\rho =$

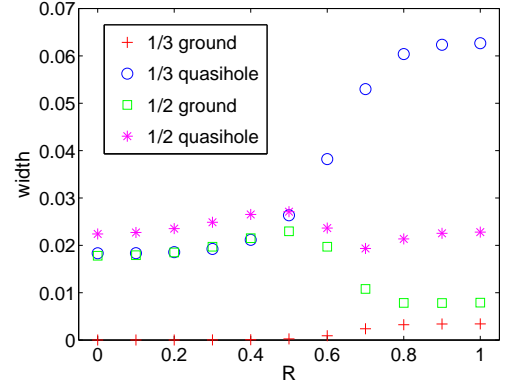


FIG. S3. The energy splittings of the nearly degenerate ground states, as well as of quasihole states for 1/3 and 1/2 fillings.

$d^{-1} \sum_{i=1}^d |\psi_i\rangle\langle\psi_i|$, where d is the number of (quasi-) degenerate ground states $\{|\psi_i\rangle\}$. The N particles are divided into two groups A and B with N_A and N_B particles. The reduced density matrix $\rho_A = \text{Tr}_B \rho$ is obtained by tracing out the particles in B . In the PES, we plot the eigenvalues $\exp(-\xi)$ of ρ_A versus the momenta of corresponding eigenstates. For the Laughlin and the Moore-Read Pfaffian wave functions, the counting of quasihole states can be derived from a generalized Pauli principle [30]. The counting of ground states and quasihole states in the FCI can be deduced from the FQH to FCI mapping developed by Bernevig and Regnault [10], which relates the degeneracy $\mathcal{N}_{\text{FQH}}(K_x, K_y)$ of low energy FQH states in the (K_x, K_y) momentum sector and the approximate degeneracy $\mathcal{N}_{\text{FCI}}(K_x, K_y)$ for the FCI case via the following equation

$$\mathcal{N}_{\text{FCI}}(K_x, K_y) = \sum_{K'_x, K'_y=0}^{N-1} \delta_{K'_x \bmod N_{x0}, K_x} \times \delta_{K'_y \bmod N_{y0}, K_y} \frac{N_{x0} N_{y0}}{N_0} \mathcal{N}_{\text{FQH}}(K'_x, K'_y) \quad (\text{S2})$$

where $N_{x0} = \text{GCD}(N, N_x)$, $N_{y0} = \text{GCD}(N, N_y)$ and $N_0 = \text{GCD}(N, N_\Phi)$ (GCD denotes the greatest common divisor).

The generalized Pauli principle does not apply in general composite fermion states. But we can still directly compare the energy spectrum of a FQH system on torus and its counterpart in a FCI to check the validity of Eq. (S2). In Fig. S4, we show energy spectra of H_2 with $N = 9$, $N_x = 4$ and $N_y = 6$ at $R = 0.0, 0.5$ and 1.0 and the energy spectra of 9 electrons and 24 fluxes on torus with Coulomb interaction, which correspond to 1/3 states with 3 quasiparticles (namely composite fermions in the second level). We find that these spectra also evolve continuously from the Hofstadter limit to the checkerboard limit as shown in Fig. S4. In Fig. S5 and S6, we show the energy spectra of H_2 at filling factor 2/5

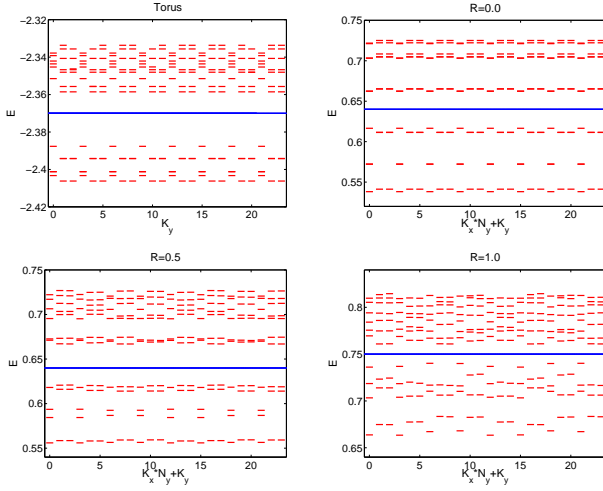


FIG. S4. 1/3 quasiparticle energy spectra on torus and on lattice at $R = 0.0, 0.5$ and 1 . The number of states below the blue lines obey the FQH to FCI mapping in Eq. (S2).

with $N = 8$, $N_x = 4$, $N_y = 5$ and $N = 10$, $N_x = 5$, $N_y = 5$. For $N = 8$, we see 5 quasi-degenerate states and a gap at each R . For $N = 10$, the 5 quasi-degenerate states all appear in the $(0, 0)$ momentum sector. The gap survives at small values of R but collapses at $R \sim 0.7$.

KAGOME LATTICE MODEL

For the triangular lattice model shown in Fig. S7 (a), each unit cell contains sixteen lattice sites labeled by (μ, ν) where $\mu, \nu \in \{0, 1, 2, 3\}$. The index of a site is defined as $i = \mu + 4\nu$ which increases from left to right and then bottom to top. We define an interpolating Hamiltonian $H_{\text{kt}}(R) = RH_{\text{kag}} + (1 - R)H_{\text{tri}}$. In the Hofstadter Hamiltonian $H_{\text{tri}} = -\sum_{\mu\nu, \sigma\rho} t_{\mu\nu, \sigma\rho} c_{\mu\nu}^\dagger c_{\sigma\rho}$, $c_{\mu\nu}^\dagger$ is the creation operator on the site (μ, ν) and only nearest-neighbor hoppings are used, *i.e.*, $t_{\mu\nu, \sigma\rho}$ is non-zero only if $\mu = \sigma \pm 1, \nu = \rho$ or $\mu = \sigma, \nu = \rho \pm 1$ or $\mu = \sigma \mp 1, \nu = \rho \pm 1$. Note that μ is defined modulo 4. The hopping amplitudes $t_{\mu\nu, \mu+1\nu}$, $t_{\mu\nu, \mu\nu+1}$, and $t_{\mu\nu, \mu-1\nu+1}$ are $\exp(i\phi_{\mu\nu}^{\text{I}})$, $\exp(i\phi_{\mu\nu}^{\text{II}})$, and $\exp(i\phi_{\mu\nu}^{\text{III}})$, respectively. The other components can be fixed by requiring the full Hamiltonian to be Hermitian. The phases arrays $\phi_{\mu\nu}^{\text{I}}$, $\phi_{\mu\nu}^{\text{II}}$ and $\phi_{\mu\nu}^{\text{III}}$ are given by

$$\begin{aligned} \phi_{0,0}^{\text{I}} &= 0 & \phi_{0,1}^{\text{I}} &= 0 & \phi_{0,2}^{\text{I}} &= 0 & \phi_{0,3}^{\text{I}} &= 0 \\ \phi_{1,0}^{\text{I}} &= 0 & \phi_{1,1}^{\text{I}} &= 0 & \phi_{1,2}^{\text{I}} &= 0 & \phi_{1,3}^{\text{I}} &= 0 \\ \phi_{2,0}^{\text{I}} &= 0 & \phi_{2,1}^{\text{I}} &= 0 & \phi_{2,2}^{\text{I}} &= 0 & \phi_{2,3}^{\text{I}} &= 0 \\ \phi_{3,0}^{\text{I}} &= 0 & \phi_{3,1}^{\text{I}} &= \frac{3\pi}{2} & \phi_{3,2}^{\text{I}} &= \pi & \phi_{3,3}^{\text{I}} &= \frac{\pi}{2} \end{aligned}$$

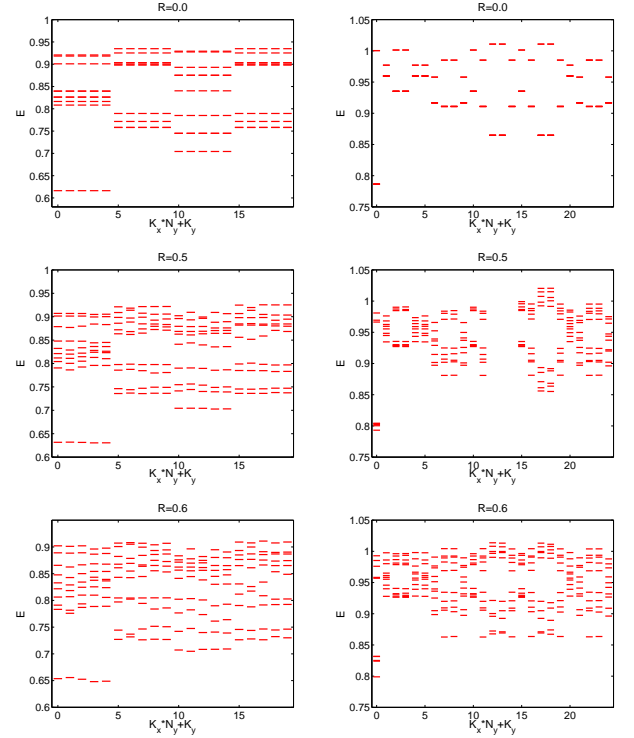


FIG. S5. 2/5 FQH ground state spectra of $N = 8$, $N_x = 4$, $N_y = 5$ (left) and $N = 10$, $N_x = 5$, $N_y = 5$ (right) at $R = 0.0, 0.5$ and 0.6 . In the left column, there are 5 quasi-degenerate states in each panel at $(K_x, K_y) = (0, 0), (0, 1), (0, 2), (0, 3)$ and $(0, 4)$. In the right column, the quasi-degenerate states all appear in the $(K_x, K_y) = (0, 0)$ sector and interaction causes splittings at $R \neq 0$.

$$\begin{aligned} \phi_{0,0}^{\text{II}} &= 0 & \phi_{0,1}^{\text{II}} &= 0 & \phi_{0,2}^{\text{II}} &= 0 & \phi_{0,3}^{\text{II}} &= 0 \\ \phi_{1,0}^{\text{II}} &= \frac{\pi}{8} & \phi_{1,1}^{\text{II}} &= \frac{\pi}{8} & \phi_{1,2}^{\text{II}} &= \frac{-\pi}{8} & \phi_{1,3}^{\text{II}} &= \frac{\pi}{8} \\ \phi_{2,0}^{\text{II}} &= \frac{\pi}{4} & \phi_{2,1}^{\text{II}} &= \frac{\pi}{4} & \phi_{2,2}^{\text{II}} &= \frac{-\pi}{4} & \phi_{2,3}^{\text{II}} &= \frac{\pi}{4} \\ \phi_{3,0}^{\text{II}} &= \frac{3\pi}{8} & \phi_{3,1}^{\text{II}} &= \frac{3\pi}{8} & \phi_{3,2}^{\text{II}} &= \frac{3\pi}{8} & \phi_{3,3}^{\text{II}} &= \frac{3\pi}{8} \\ \phi_{0,0}^{\text{III}} &= \frac{\pi}{16} & \phi_{0,1}^{\text{III}} &= \frac{\pi}{16} & \phi_{0,2}^{\text{III}} &= \frac{\pi}{16} & \phi_{0,3}^{\text{III}} &= \frac{\pi}{16} \\ \phi_{1,0}^{\text{III}} &= \frac{3\pi}{16} & \phi_{1,1}^{\text{III}} &= \frac{3\pi}{16} & \phi_{1,2}^{\text{III}} &= \frac{3\pi}{16} & \phi_{1,3}^{\text{III}} &= \frac{3\pi}{16} \\ \phi_{2,0}^{\text{III}} &= \frac{5\pi}{16} & \phi_{2,1}^{\text{III}} &= \frac{5\pi}{16} & \phi_{2,2}^{\text{III}} &= \frac{5\pi}{16} & \phi_{2,3}^{\text{III}} &= \frac{5\pi}{16} \\ \phi_{3,0}^{\text{III}} &= \frac{25\pi}{16} & \phi_{3,1}^{\text{III}} &= \frac{-17\pi}{16} & \phi_{3,2}^{\text{III}} &= \frac{-9\pi}{16} & \phi_{3,3}^{\text{III}} &= \frac{-\pi}{16} \end{aligned}$$

The kagome lattice Hamiltonian [4] is given by $H_{\text{kag}} = -\sum_{\mu\nu, \sigma\rho} \tilde{t}_{\mu\nu, \sigma\rho} c_{\mu\nu}^\dagger c_{\sigma\rho} = \sum_{\vec{k}, i, j} \mathcal{H}_{ij}(\vec{k}) c_i^\dagger(\vec{k}) c_j(\vec{k})$ ($i = \mu + 4\nu$ and $j = \sigma + 4\rho$). The non-zero components of \mathcal{H}_{ij} are $H_{02} = -2(t_1 \cos(k_x/2) + t_2 \cos(k_y - k_x/2))$, $H_{28} = -2(t_1 \cos((k_y - k_x)/2) + t_2 \cos((k_x + k_y)/2))$, $H_{80} = -2(t_1 \cos(k_y/2) + t_2 \cos(k_x - k_y/2))$, and those related to them via Hermitian conjugation, where $t_1 = 1.0 + 0.28i$ and $t_2 = -0.3 - 0.2i$.

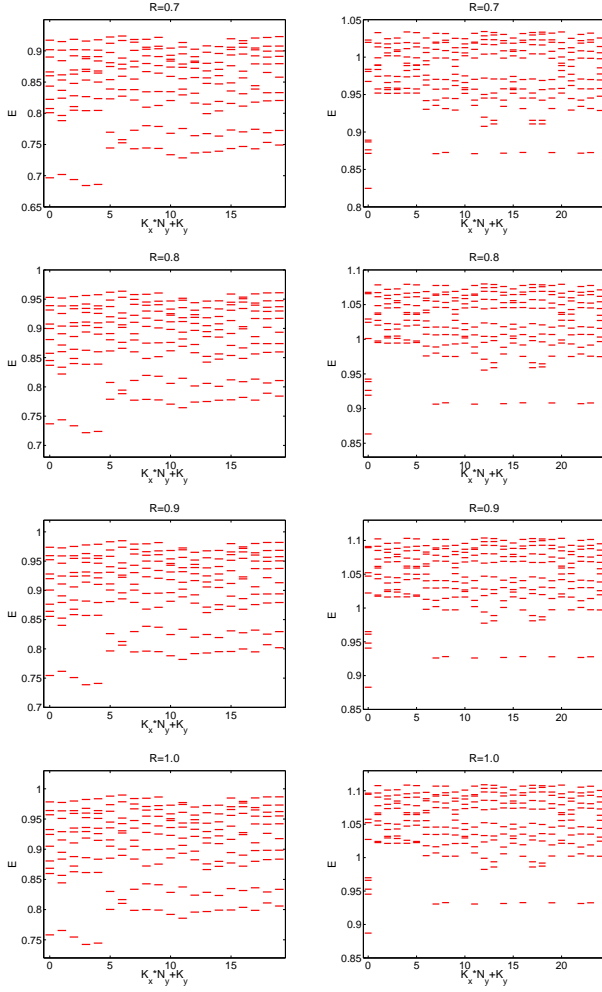


FIG. S6. $2/5$ FQH ground state spectra of $N = 8$, $N_x = 4$, $N_y = 5$ (left) and $N = 10$, $N_x = 5$, $N_y = 5$ (right) at $R = 0.7$, 0.8 , 0.9 and 1 . In the left column, there are 5 quasi-degenerate states in each panel at $(K_x, K_y) = (0, 0), (0, 1), (0, 2), (0, 3)$ and $(0, 4)$. In the right column, the quasi-degenerate states all appear in the $(K_x, K_y) = (0, 0)$ sector and interaction causes substantial splittings at large R .

Fig. S7 (b) shows the band structures at $R = 0.0, 0.5$ and 1.0 . Fig. S8 shows the Berry curvature at $R = 0.0, 0.5$ and 1.0 .

We use a two body Hamiltonian $H_2 = \sum_{[i,j]} U_{ij} \hat{n}_i \hat{n}_j$ at $\nu = 1/3$ and a three body Hamiltonian $H_3 = \sum_{[i,j,k]} V_{ijk} \hat{n}_i \hat{n}_j \hat{n}_k$ at $\nu = 1/2$, where $\hat{n}_i = c_i^\dagger c_i$ is the particle number operator on site i , $U_{ij} = 0.5/r_{ij}^2$ and $V_{ijk} = 0.5/(r_{ij}r_{jk}r_{ki})^2$, where r_{ij} is the distance between the sites i and j . The summation in H_2 is over all pairs i, j for which $r_{ij} \leq 1/2$ and that in H_3 is over all combinations of i, j, k for which $r_{ij}, r_{jk}, r_{ki} \leq 1/8$ and $r_{ij}r_{jk}r_{ki} \leq 1/2$. All distances here are in units of the lattice constant of the magnetic unit cell.

Fig. S9 shows the the energy spectra at $1/3$ ($N = 8$, $N_x = 4$ and $N_y = 6$) and $1/2$ ($N = 10$, $N_x = 4$ and

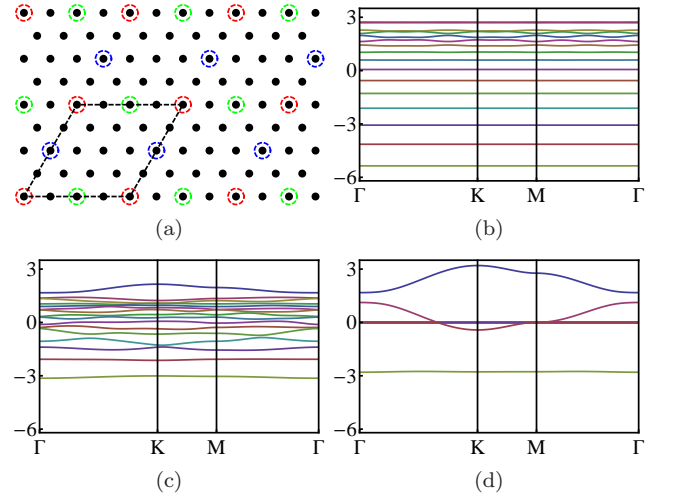


FIG. S7. Lattice model and band structure for the kagome lattice model. Fig. (a) shows the lattice. In panel (a), the black dots show the lattice sites in a triangular Hofstadter lattice with flux $\pi/16$ in each triangle. The dashed lines mark a magnetic unit cell, which contains 16 sites. The sites marked by the dashed circles form a kagome lattice where the three different colors represent the three sublattices. Panels (b-d) shows the band structures at different values of R ($0.0, 0.5$ and 1 correspondingly) along the contour $\Gamma \rightarrow K \rightarrow M \rightarrow \Gamma$ in the momentum space.

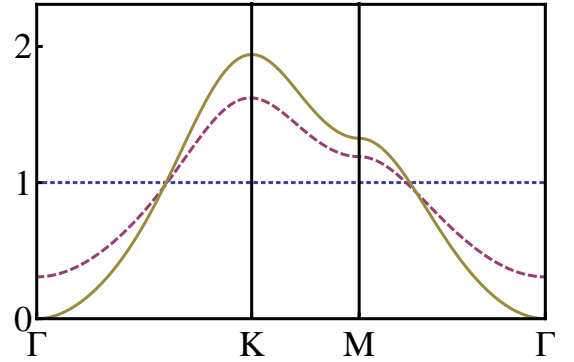


FIG. S8. Berry curvature in the kagome lattice model at different \mathbf{k} -points with $R = 0.0, 0.5$ and 1.0 (dotted, dashed and solid lines respectively).

$N_y = 5$) fillings with $R = 0.0, 0.5$ and 1.0 . For $1/3$ filling, we observe 3 quasi-degenerate states at $(K_x, K_y) = (0, 0), (0, 2)$ and $(0, 4)$, while 6 quasi-degenerate states are found at $1/2$ filling: one for $(K_x, K_y) = (0, 0)$ or $(2, 0)$ and two for $(1, 0)$ or $(3, 0)$. These are the same as in the checkerboard model.

Fig. S10 shows the quasihole spectra with $N = 7$, $N_x = 4$ and $N_y = 6$ ($N = 10$, $N_x = 3$ and $N_y = 7$), which corresponds to a $\nu = 1/3$ ($\nu = 1/2$) state with three (two) quasiholes, and we observe 12 (6) low energy states in each momentum sector for $1/3$ ($1/2$) filling. These are also the same as in the checkerboard lattice model.

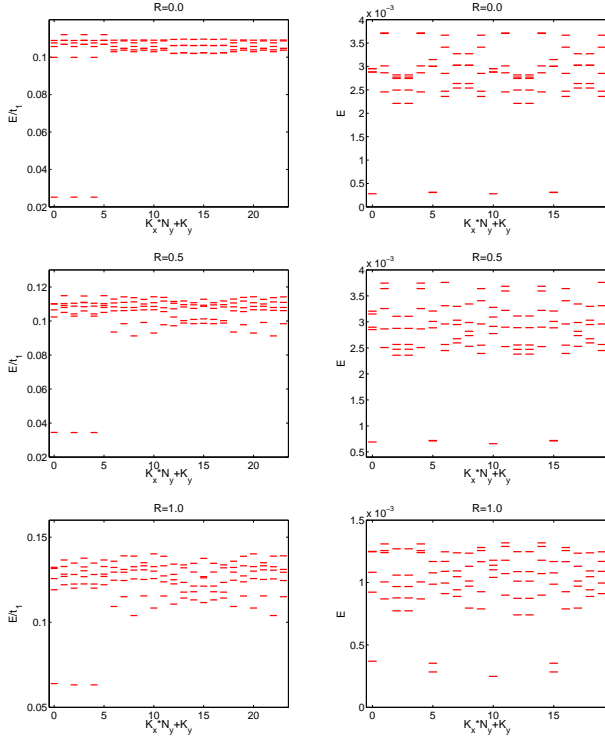


FIG. S9. Energy spectra at filling 1/3 (left) and 1/2 (right) for $R = 0.0, 0.5$ and 1.0 (top to bottom). In the left panels, there are 3 quasi-degenerate states at $(K_x, K_y) = (0,0)$, $(0,2)$ and $(0,4)$. In the right panels, there are 6 quasi-degenerate states: one each at $(K_x, K_y) = (0,0)$ or $(2,0)$, and two for $(1,0)$ or $(3,0)$. The system size is 4×6 (4×5) for 1/3 (1/2) filling.

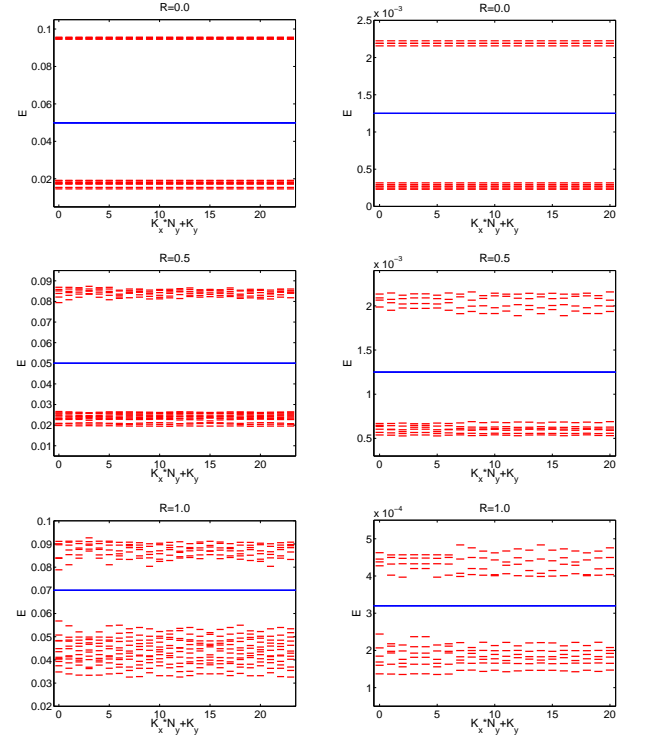


FIG. S10. Quasihole spectra at 1/3 (left) and 1/2 (right) fillings at $R = 0.0, 0.5$ and 1.0 (top to bottom). There are 12 (6) states in the low energy manifold (below the blue lines) in each momentum sector for the left (right) column.